AGU PUBLICATIONS

JGR

Journal of Geophysical Research: Space Physics

RESEARCH ARTICLE
10.1002/2015JA021621

Key Points:
- Intensity between Saturn and D ring is lower than in Saturn's proton belts
- Intensity over the D ring might be comparable to Saturn's known belts
- Proton intensity is limited by neutral density, not diffusion as in known belts

Correspondence to:
P. Kollmann,
Peter.Kollmann@jhuapl.edu

Citation:
Kollmann, P., E. Roussos, A. Kotova, J. F. Cooper, D. G. Mitchell, N. Krupp, and C. Paranicas (2015), MeV proton flux predictions near Saturn's D ring, *J. Geophys. Res. Space Physics*, *120*, 8586–8602, doi:10.1002/2015JA021621.

Received 25 JUN 2015
Accepted 22 SEP 2015
Accepted article online 28 SEP 2015
Published online 24 OCT 2015

MeV proton flux predictions near Saturn's D ring

P. Kollmann[1], E. Roussos[2], A. Kotova[2,3], J. F. Cooper[4], D. G. Mitchell[1], N. Krupp[2], and C. Paranicas[1]

[1]The Johns Hopkins University, Applied Physics Laboratory, Laurel, Maryland, USA, [2]Max Planck Institute for Solar System Research, Göttingen, Germany, [3]Université Paul Sabatier Toulouse III, UPS-OMP, IRAP, Toulouse, France, [4]NASA Goddard Space Flight Center, Greenbelt, Maryland, USA

Abstract Radiation belts of MeV protons have been observed just outward of Saturn's main rings. During the final stages of the mission, the Cassini spacecraft will pass through the gap between the main rings and the planet. Based on how the known radiation belts of Saturn are formed, it is expected that MeV protons will be present in this gap and also bounce through the tenuous D ring right outside the gap. At least one model has suggested that the intensity of MeV protons near the planet could be much larger than in the known belts. We model this inner radiation belt using a technique developed earlier to understand Saturn's known radiation belts. We find that the inner belt is very different from the outer belts in the sense that its intensity is limited by the densities of the D ring and Saturn's upper atmosphere, not by radial diffusion and satellite absorption. The atmospheric density is relatively well constrained by EUV occultations. Based on that we predict an intensity in the gap region that is well below that of the known belts. It is more difficult to do the same for the region magnetically connected to the D ring since its density is poorly constrained. We find that the intensity in this region can be comparable to the known belts. Such intensities pose no hazard to the mission since Cassini would only experience these fluxes on timescales of minutes but might affect scientific measurements by decreasing the signal-to-contamination ratio of instruments.

1. Introduction

In this paper we study energetic protons very close to Saturn. Our focus is on spacecraft and instrument-penetrating protons in the 10–100 MeV range but we extend our study down to keV energies. We consider the gap region between Saturn's dense atmosphere and the inner edge of the D ring, in the equatorial plane between 1.02 and $1.06R_S$ from Saturn's center (Saturn radius $R_S = 60,268$ km). Also, the D ring extending out to $1.24R_S$ and magnetic field lines connected to this ring are considered.

During Saturn orbit insertion, the INCA camera, part of the MIMI instrument package [*Krimigis et al.*, 2004] of the Cassini spacecraft, was put in a unique location, from where it could detect energetic neutral atoms (ENAs) with energies of tens of keV coming from the gap between the D ring and Saturn's atmosphere [*Krimigis et al.*, 2005]. This measurement indicates the presence of trapped keV ions in that region. It is reasonable to assume that this region is also populated by MeV ions similar to Saturn's known ion radiation belts [*Krimigis et al.*, 1983; *Armstrong et al.*, 2009; *Roussos et al.*, 2011]. During closest approach, Cassini crossed field lines that map to an equatorial distance of $1.42R_S = 86$ Mm in the equatorial plane, which lies in the C ring, near the Maxwell gap. Energetic particle intensities measured by the MIMI/LEMMS instrument were low compared to the radiation belts [*Krimigis et al.*, 2005] (Figure 1). It is an active subject of research whether species and energies of the particles are correctly determined or if the measurements result from cosmic ray or other contamination that produces false detector counts. In comparison, the main telescope of the University of Chicago experiment [*Simpson et al.*, 1980] on board of Pioneer 11 counted MeV electrons and tens of MeV protons with rates that were low but significant [*Chenette et al.*, 1980; *Cooper et al.*, 1985].

No spacecraft, including Cassini, has reached the radial distance of the D ring. Its inner part is almost completely transparent to light and so tenuous that its optical depth has not been constrained accurately [*Hedman et al.*, 2007]. It is therefore possible that MeV ions coexist with the ring, similar as how they survive in the E and G rings.

The known ion belts are located between about 2 and $5R_S$, see black curve in Figure 1. They are collocated with the orbits of several of the icy moons. Unlike at Jupiter, the magnetic and spin equators are coaligned, meaning that the moons are very effective absorbers of energetic ions and isolate the belts from the rest of

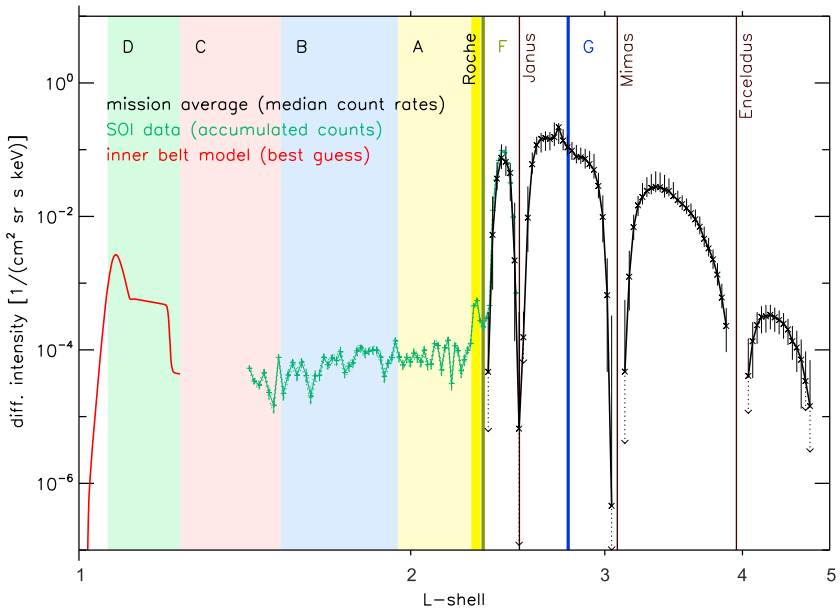

Figure 1. Compilation of measured and modeled radial intensity profiles. Black: Mission-averaged median omnidirectional intensities of the MIMI/LEMMS P7 channel, measuring protons around 27 MeV, near the magnetic equator. Error bars show the standard deviation. Green: Measurements during Cassini's first orbit. We bin counts in *L* shell and divide it by the integration time. Error bars are Poisson errors. Note detection of the Roche radiation belt in the Roche division. Intensity over the rings is likely contaminated and an upper limit. (Pioneer 11 measured $10^{-8}/(\mathrm{cm}^2\ \mathrm{sr\ s\ keV})$) [*Cooper et al.*, 1985]. Red: Best guess model of the radiation belt around the D ring for 27 MeV protons as described through sections 2 and 3.

the magnetosphere [*Roussos et al.*, 2008]. Therefore, the protons found in these belts cannot originate from the magnetosphere or the solar wind but originate primarily from cosmic ray albedo neutron decay (CRAND) [*Singer*, 1958; *Hess et al.*, 1959; *Krimigis and Armstrong*, 1982; *Cooper*, 1983; *Kollmann et al.*, 2013]. In this process, galactic cosmic rays (GCRs) [*Blasi*, 2013], typically > GeV protons, enter Saturn's magnetosphere, collide with material, the rings or planetary atmosphere, and create secondary neutrons at energies lower than the primary particle. A fraction of these beta decay to protons, become trapped by Saturn's magnetic field, and populate the belts. Since the magnetic and electric fields fluctuate stochastically, the protons undergo a stochastic motion that can be described well by radial diffusion [*Roederer*, 1970, pp. 112–132; *Schulz and Lanzerotti*, 1974, pp. 81–92; *Walt*, 1994, pp. 92–146]. Diffusion leads proton trajectories to intersect moon orbits, where they are absorbed. It is diffusion that causes a reduction in ion intensity even outside of the radial range covered by the moon throughout its orbit.

The gap region between the D ring and Saturn and D ring itself are much closer to Saturn and the source of neutrons than the known ion belts are. The magnetic field is stronger there, so that diffusive losses are expected to be weaker. It has therefore been suggested that the inner radiation belt in the gap region has a higher intensity of MeV protons than the known belts [*Cooper*, 2008; *Cooper et al.*, 2011]. These estimates were under the now questionable assumption of no absorption by atmospheric gas or ring material, which is expected to be present.

The region that magnetically connects with the gap region and D ring is of special interest to the Cassini mission. The proximal orbits scheduled for 2017 will lead the spacecraft over the rings and through the gap (Figure 2). Particles bouncing along field lines that connect to the rings will reach Cassini even though it avoids the rings themselves. Intense radiation on those field lines might affect Cassini's instrument performance. For example, the INMS instrument (measures neutral particles) [*Waite et al.*, 2006] is contaminated by energetic particles in the known radiation belts to an extent that studying this region becomes challenging [*Elrod et al.*, 2012]. Similar intensities in the inner belt could prevent in situ measurements of the exospheres of Saturn and the D ring. If the intensities are extreme, they could even affect Cassini's electronics and therefore interfere with its operations.

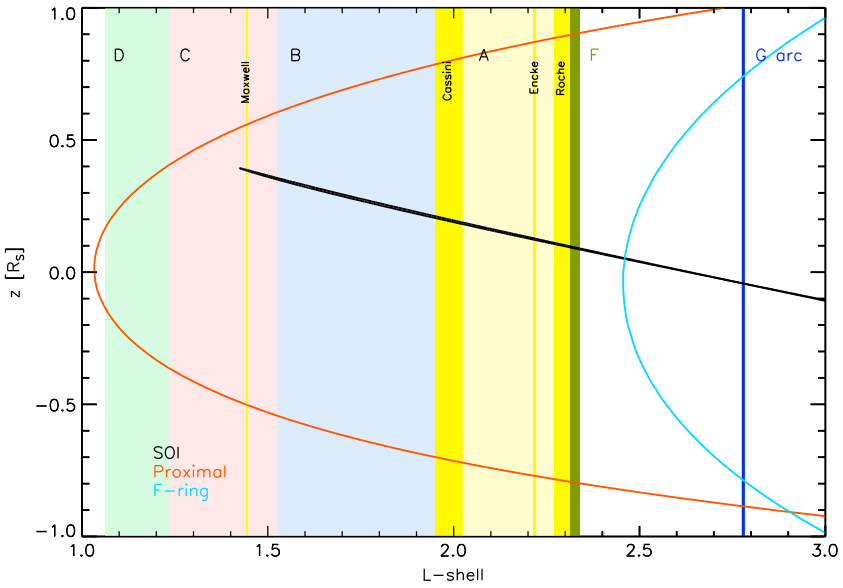

Figure 2. Cassini's first orbit (black curve) in comparison with orbits planned for the end of the mission. We show a typical proximal (red) and F ring (blue) orbit. *L* is the magnetic dipole shell, and *z* is the distance from the ring plane, both in multiples of a Saturn radius. Vertical lines and shades indicate the locations of rings and gaps.

The purpose of this paper is to establish upper limits on the expected MeV proton radiation levels. We show that the inclusion of atmospheric hydrogen gas brings down the intensity in the gap below the value present in the known belts. The intensity connected with the inner D ring is more uncertain but likely not magnitudes higher than the known belts.

This paper is structured as follows: We explain the model and our default assumptions in section 2. The relatively short section 3 presents the results. In section 4 we discuss how the results change depending on the model parameters, some of which are poorly constrained so far. We find that our modeled spectra resemble and help understand measurements in the magnetosphere. This is discussed in Appendix A.

2. Model

The model used in this paper is a modified version of the *Kollmann et al.* [2013] model, which we used to successfully reproduce Saturn's known proton belts. We numerically solve either of the two following differential equations for the phase space density, f, which is defined here as particles per volume in real and momentum space (Note that this is different from a definition that uses velocity space.). Phase space density, f, is related to the differential intensity, j, which is particles per time, energy interval, area, and solid angle, as $f = j/p^2$ with the momentum p.

$$\frac{\mathrm{d}f_{\mu,K}(L)}{\mathrm{d}t} = S + \hat{D}f \tag{1}$$

$$\frac{\mathrm{d}f_{L,\alpha}(E)}{\mathrm{d}t} = S + \hat{E}f + \hat{C}f \tag{2}$$

$f_{x,y}(z)$ means that, while f depends on x and y, these parameters are kept fixed and that the differential equation describes the dependence of f on z. Specifically, μ and K are the first and second adiabatic invariants [*Roederer*, 1970, pp. 19–23, pp. 46–52; *Walt*, 1994, pp. 36–50] (Table 1), and E is the particle kinetic energy. The L shell gives the distance in multiples of R_S of the equatorial crossing point of the magnetic field line occupied by the particle. The term α is the equatorial pitch angle, which is the angle of the proton velocity vector relative to the magnetic field direction at the magnetic equator. $\mathrm{d}f/\mathrm{d}t$ is the overall change of phase space density per time. For simplicity, we assume a steady state: $\mathrm{d}f/\mathrm{d}t = 0$. S is a source rate (gain of f per time). $\hat{D}f$ describes radial diffusion, $\hat{E}f$ particle loss by energy loss, and $\hat{C}f$ charge exchange. The $\hat{}$ symbol is used

Table 1. Explanation of Variables and Abbreviations Used Throughout This Paper

α	equatorial pitch angle (angle of proton velocity relative to magnetic field at magnetic equator)
B	magnetic field
B_m	magnetic field at mirror latitude λ_m
$\widehat{C}f$	charge exchange rate (loss of phase space density per time, equation 9)
CRAND	cosmic ray albedo neutron decay
D	diffusion coefficient
$\mathrm{d}E/\mathrm{d}x$	energy loss per distance in a given material (stopping power)
$\mathrm{d}f/\mathrm{d}t$	overall change of phase space density per time (equations (1) and (2))
$\widehat{D}f$	L shell diffusion rate (change of phase space density per time, equation (3))
E	energy
E_0	reference energy for source (see section 2.1)
E_c	energy cutoff of galactic cosmic rays (minimum energy required by the Størmer limit to enter an L shell)
E_E	energy cutoff of source rate (E_E=120 MeV)
$\widehat{E}f$	energy loss rate (change of phase space density per time, equation (4))
ENA	energetic neutral atom
f	phase space density (protons per volume in real and momentum space)
GCR	galactic cosmic ray
H	vertical extent of D ring
I	integral proton intensity between 1 and 60 MeV, averaged over all directions (protons per time and area)
I_{max}	highest value of I measured at Saturn ($I_{\mathrm{max}} = 6 \times 10^8 \mathrm{m}^{-2}\mathrm{s}^{-1}$ at $L = 2.6$)
j	differential intensity (protons per time, area, solid angle, and energy interval)
K	second adiabatic invariant $K = \int_{-\lambda_m}^{+\lambda_m} \sqrt{B_m - B}\,\mathrm{d}s$ with ds along the magnetic field B
L	dimensionless dipole L shell (equal to radius in R_S in equatorial plane, follows magnetic dipole to higher latitudes)
λ_m	magnetic mirror latitude at which a bouncing particle turns around
m	exponent of source rate S
M	mass of one water molecule
Mm	$10^6 m$
μ	first adiabatic invariant $\mu = E(E + 2mc^2)/(2mc^2 B)\sin^2\alpha$
$\langle n \rangle$	number density of neutral particles in D ring or exosphere, averaged over periodic proton motion (equation (6))
$\langle n \rangle_r$	number density of water molecules, averaged throughout a D ring with thickness H (equation (5))
n	exponent of diffusion coefficient D
$\overline{n}$	D ring grain size distribution (ice grains of given radius per volume and radius interval)
p	proton momentum
PSD	phase space density (protons per volume in real and momentum space)
r	D ring grain size radius
R_S	Saturn radius (60,268 km)
ρ	mass density of water ice (mass per volume)
S	source rate (gain of phase space density per time)
σ	charge exchange cross section (area)
T_B	bounce time
T_r	time a proton spends in D ring per bounce period
τ	optical depth of D ring (equation (7))
v	proton velocity

to mark operators that act on f, meaning that the result might depend on derivatives of f in L or E. Detailed explanations of the terms are given below. Table 1 summarizes the major variables and abbreviations of this paper.

Our solutions of equations (1) and (2) are computed by the commercial software Mathematica [*Wolfram Research*, 2012]. We always check if the solution fulfills the differential equation and the boundary conditions.

2.1. Source and Diffusion

The term S in equations (1) and (2) is the source rate. We describe it using the parameters that we determined from the known radiation belts [*Kollmann et al.*, 2013]. The source scales as $S \propto 10^{63}(3.5/\mathrm{L})^{-m}\mathrm{s}^2/(\mathrm{kg}^3\mathrm{m}^6)$ over L shell with an exponent $m = 3$. The dependence of the source on energy E goes as the measured ion spectrum in 2 to $5R_S$ region: for <8 MeV we use a power law $S \propto (E/E_0)^{-3.9}$ with $E_0 = 1$ keV. For higher energies, we use a log-log scale parabola centered at 12.4 MeV with a rapid cutoff at $E_E = 120$ MeV.

Equation (1) is the extreme case where the source is balanced only by radial diffusion that drives protons into other regions. $\hat{D}f$ describes diffusion of the phase space density $f_{\mu,K}(L)$ in L shell.

$$\hat{D}f = L^2 \frac{\partial}{\partial L}\left(\frac{D}{L^2}\frac{\partial f}{\partial L}\right) \tag{3}$$

D is the diffusion coefficient. We use $D(L) = 0.3 \times 10^{-9}(L/3.5)^n 1/s$ with an exponent $n = 10$ [*Kollmann et al.*, 2013]. Equation (1) can be solved for fixed first and second adiabatic invariants μ and K. These quantities depend on particle energy and pitch angle but, contrary to them, are constants during slow radial motions [*Walt*, 1994, pp. 36–50].

2.2. Energy Loss and Charge Exchange

Equation (2) is the other extreme where radial diffusion is negligible and losses occur solely because of interactions of the protons with material. $\hat{E}f$ represents the change in $f_{L,\alpha}(E)$ of protons of a given energy E due to energy loss in the atmosphere and in the D ring. Equation (2) can be solved for each L and equatorial pitch angle α separately. Atmosphere and ring interactions are each represented by a term of the following form [*Kollmann et al.*, 2013]

$$\hat{E}f = -\frac{v}{p^2}\frac{\partial}{\partial E}\left(p^2 f \frac{\mathrm{d}E}{\mathrm{d}x}\right) \tag{4}$$

where v is the proton velocity and p is the momentum. The energy loss per distance in a material $\mathrm{d}E/\mathrm{d}x$ is available as tabulated values and does not have to be considered as derivative of a function. $\hat{E}f$ can be either positive or negative, i.e., causes either a decrease or an increase of the phase space density, depending on the shape of the proton spectrum f and on $\mathrm{d}E/\mathrm{d}x$ (Results are shown in Figure 4.).

Equation (4) assumes that the protons undergo a continuous energy loss per traversed distance $\mathrm{d}E/\mathrm{d}x$ and over their whole trajectory are subject to a constant density $\langle n\rangle$ (molecules per volume). We use values for $\mathrm{d}E/\mathrm{d}x$ from *Berger et al.* [2005]. They scale approximately linearly with the density of the target particles even if their impact parameter is larger than the nominal radius of the target molecule. A minor correction arises because the ionization energy changes with target particle distance, but we neglect this here. The assumption of continuous energy loss works well for a gas. As we show in Appendix B, it is also sufficient to describe MeV protons interacting with mm to μm sized water ice grains. For lower energies or much larger grains, the discrete energy loss and probability to hit a grain need to be taken into account [*Kollmann et al.*, 2011].

For equatorially mirroring particles whose whole gyration is within the atmosphere, $\langle n\rangle$ is simply the density at the equator. For bouncing particles, the density needs to be averaged over the trajectory. The distance to Saturn's center, h, of bouncing particles changes with latitude λ as $h = L\cos^2\lambda$. This change is much stronger than Saturn's oblateness (polar radius is $0.90R_S$) [*Seidelmann et al.*, 2007] or the atmospheric asymmetries around the exobase ($< 0.01R_S$) [*Koskinen et al.*, 2013]. More field-aligned particles will therefore experience stronger losses, yielding lower intensities. This means that the pitch angle distribution of particles whose motion is completely within the atmosphere will peak for equatorially mirroring particles. Since we are aiming for upper limit intensities, we will use the equatorial density for all pitch angles.

For the D ring, we assume that the molecules of the ice grains are homogenously distributed over the ring. The molecular density $\langle n\rangle_r$ of the ring is related to the grain size distribution $\overline{n}$ (grains of radius r per volume and radius interval) as

$$\langle n\rangle_r = \frac{\rho}{M}\int_{r_{\min}}^{r_{\max}} \frac{4\pi}{3}\overline{n}r^3\mathrm{d}r \tag{5}$$

with the mass density ρ of water ice and the mass M of a water molecule. The different kinds of densities used throughout this section are summarized in Table 1. We assume that $\overline{n}$ is spatially constant throughout the D ring with vertical extend H across the equatorial plane. The density averaged over the proton trajectory is then

$$\langle n\rangle = \langle n\rangle_r \frac{T_r}{T_B} \tag{6}$$

with the time T_r spent in the ring and the bounce time T_B. Note that this is different from the ratio of latitudes.

This expression can be related to the optical depth τ, which can be calculated as

$$\tau = \int_{r_{\min}}^{r_{\max}} \overline{n} H \pi r^2 \mathrm{d}r \tag{7}$$

Forcing equation (7) into (6) yields

$$\langle n \rangle = \frac{4\rho\tau T_r}{3HMT_B} \frac{\int_{r_{\min}}^{r_{\max}} r^3 \tilde{n} \mathrm{d}r}{\int_{r_{\min}}^{r_{\max}} r^2 \tilde{n} \mathrm{d}r} \tag{8}$$

The grain size distribution can be expressed as a product: $\overline{n} = n_0 \tilde{n}(r)$. The advantage of equation (8) over (6) is that it only depends on the shape $\tilde{n}$ of the size distribution, not its absolute value. The density $\langle n \rangle$ has only a weak explicit dependence on the ring thickness H since $T_r \propto H$ is approximately true for a thin ring. (The ring thickness is implicitly included via the optical depth τ.) We assume here $H = 100$ m, about an order of magnitude more than the A ring [*Colwell et al.*, 2009a].

The most field-aligned equatorial pitch angle at the outer edge of the D ring is 40°. Particles with smaller pitch angles have their mirror point with the dense atmosphere and are lost. We calculate the density $\langle n \rangle$ for this angle. More equatorial particles will experience higher densities since they will spend more time T_r within the ring, resulting in lower intensities.

An exception is particles that mirror very close to the magnetic equator. Since the magnetic equator is offset from the ring plane (by $0.036R_S$) [*Burton et al.*, 2010], these particles will not suffer strong losses. In time, they can lose energy from interaction with the ring exosphere. At low energies, pitch angle scattering in the exosphere will become important and eventually drive them into the ring. If this is slow compared to the source rate, particles will accumulate to high intensities. Since these protons will by definition not bounce up to Cassini's latitude, they cannot be measured in situ or cause problems to Cassini or its instruments. In principle, they might be detectable remotely as ENAs. MIMI/INCA will measure them in case the intensity at tens of keV is high enough.

On top of energy loss, interaction with gas and ice scatters the protons (causing pitch angle diffusion) and broadens their energy distribution (straggling, causing energy diffusion). We do not consider this here since it turns out that this is negligible for MeV protons [*Kollmann et al.*, 2013].

$\widehat{C}f$ accounts for charge exchange. This process converts protons into energetic neutral atoms (ENAs) that escape the Saturn system.

$$\widehat{C}f = -\sigma \langle n \rangle v f \tag{9}$$

where σ is the charge exchange cross section. We use values for protons charge exchanging with H from *Lindsay and Stebbings* [2005] and of H_2 from *Barnett et al.* [1990]. They provide values extending to about 220 keV, and we extrapolate beyond that energy. The error from this extrapolation does not play a role since at these energies charge exchange becomes negligible compared to energy loss.

Charge exchange is only important for energies below several 100 keV and is only included for completeness. It is possible that the charge exchange losses are compensated or even countered by another process: ENAs can be stripped of an electron again when colliding with a neutral particle [*Barnett et al.*, 1990]. The ENAs do not have to be produced locally but can also originate from other locations in the inner belt or the magnetosphere. It was suggested that the main source of keV ions in the gap region is from stripping [*Krimigis et al.*, 2005], similar to Earth's low-altitude proton belt [*Moritz*, 1972; *Gusev et al.*, 2003].

Protons passing ice grains can become neutralized [*Kreussler and Sizmann*, 1982]. This additional sink is not considered here.

2.3. Atmospheric and D Ring Model

The gas in the gap region mainly originates from Saturn's atmosphere but might have contributions from the rings. The region we are considering include parts of the thermosphere and exosphere, separated by the exobase around $1.05R_S$ [*Koskinen et al.*, 2013]. We use values that approximate the Cassini project's engineering atmosphere model initially developed in 2010 (D. Strobel, private communication). It was subsequently validated by solar EUV occultations described in *Koskinen et al.* [2013] and stellar EUV occultations in [*Koskinen et al.*, 2015], all observed with the UVIS instrument on Cassini [*Esposito et al.*, 2004]. The dominating species close to Saturn is H_2. We assume an equatorial density of $4 \times 10^{16} \mathrm{m}^{-3}$ at an altitude of $1.02R_S$. Inward of this

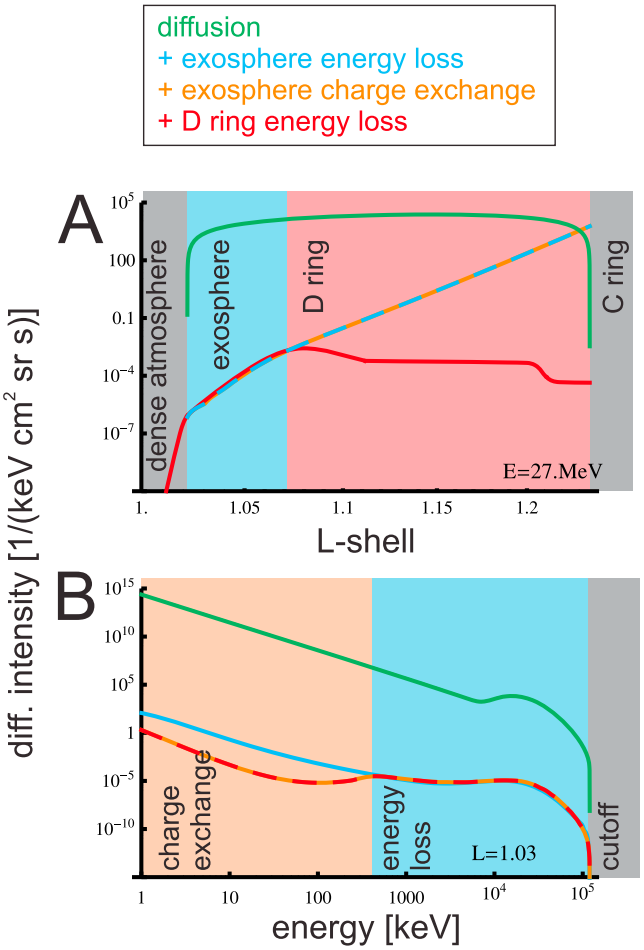

Figure 3. Model results for different processes included. (a) Radial intensity profile of 27 MeV protons. (b) Energy spectra at $L = 1.03$. Green: Assuming only radial diffusion and no material in and around the D ring. Blue and Orange: Assuming exospheric gas densities that approximate the Cassini project's engineering atmosphere. Blue considers only energy loss, orange also accounts for charge exchange. Diffusion is negligible here when these effects are present. Spectra in the D ring are not shown but resemble the blue curve. (There is no difference in Figure 3a between the blue and orange profiles since they are at an energy not affected by charge exchange.) Red: Additionally including energy loss in the D ring ice grains. (No difference in Figure 3b between red and orange spectra since they are for a location of no significant D ring density.)

altitude the density rises steeply, outward it decays exponentially to $2 \times 10^{14}\mathrm{m}^{-3}$ at $1.05R_S$. Outward of this distance, H is dominating and also decays exponentially with about the double scale length.

The optical depth of the outer D ring, between 73 and 74.5 Mm (1.21–1.24 R_S) [*Horányi et al.*, 2009], coincident with the D73 ringlet, is of the order of 10^{-3} [*Hedman et al.*, 2007]. We calculate the average density $\langle n \rangle$ using equation (8) and assume a grain radius distribution that scales as $\bar{n} \propto r^{-3}$ between 0.1 μm and 1 mm and is zero otherwise. We will discuss different densities in section 4 since the size distribution is very uncertain.

The optical depth of the inner part of the ring, between 67 and 73 Mm (1.11–1.21 R_S), is so low that it has not been well constrained to date [*Hedman et al.*, 2007]. We assume here that the density $\langle n \rangle$ in this region is 10 times lower than in the outer D ring. We neglect the embedded brighter D68 and D72 ringlets here. Inside of 67 Mm, the normalized I/F reflectance shows an exponential decay with scale length 1000 km (M. M. Hedman, private communication, 2013). We assume that the I/F profile is proportional to the density. Although I/F flattens out inside of about 64 Mm ($1.06R_S$), we assume that it keeps falling in order to get upper limit intensities.

We discuss further details of the atmosphere and D ring densities together with their uncertainties in sections 4.1 and 4.2.

2.4. Boundary Conditions

Equation (1) requires two boundary conditions. We assume $f = 0$ at $L = 1.02$, where the atmospheric density starts to rise steeply, and at $L = 1.24$, about the outer edge of the D ring. Equation (2) requires one boundary condition. We use $f = 0$ at $E_E = 120$ MeV, which is the energy where we force the source to zero (section 2.1). The value of E_E does not affect the results at energies well below it.

3. Results

3.1. Best Guess

Modeled radial intensity profiles and energy spectra using the most likely parameters can be found in Figure 3. How the model changes depending on these parameters will be discussed in section 4. Here we discuss how different physical processes affect the model results.

The green curves in Figure 3 represent the theoretical case with no material present. Figure 3a shows a radial profile at a fixed energy (near the CRAND peak), and Figure 3b an energy spectrum at a fixed location (between the dense atmosphere and the D ring). The radial profile has its maximum about in the center of the region

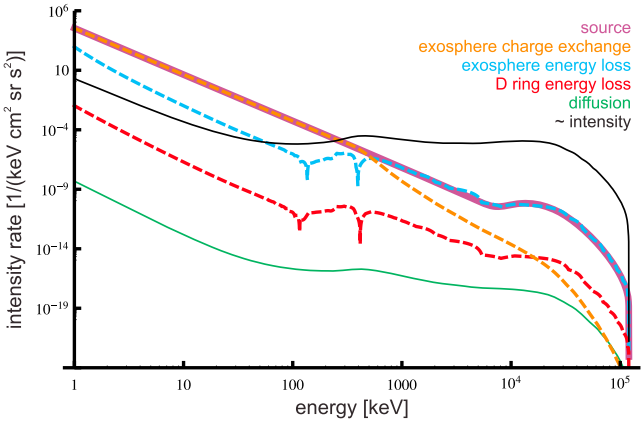

Figure 4. Absolute value of the change of intensity per time ($p^2|\mathrm{d}f/\mathrm{d}t|$) for the best model. Thick violet: Source rate $\propto S$. Dashed orange: Loss rate $\propto \tilde{C}f$ from charge exchange. Dashed blue: Intensity change resulting from energy loss ($\propto \tilde{E}f$) in the atmosphere. The intensity increases between 100 and a few hundred keV and decreases otherwise. Sign changes show as sharp dropouts. Dashed red: Energy loss in the D ring. Green: Diffusive loss rate $\propto \tilde{D}f$. Black: Proportional to the intensity spectrum for comparison.

considered and is forced to zero by strong losses at the edges. (The maximum appears as a plateau since Figure 3 spans many orders of magnitude, but the contrast between the peak and the regions just outside where the steep losses occur is about a factor of 10.) Radial diffusion drives the protons to these edges and therefore limits the overall intensity. Since diffusion is treated as energy independent, the energy spectrum has the same shape as the source function.

The orange and blue curves assume a gas density that approximates the engineering atmosphere model. It can be seen in Figure 3a that the intensity increases radially outward as the gas density decreases. The blue spectrum in Figure 3b includes only energy loss in the atmospheric gas. Energy loss washes out the CRAND peak around 10 MeV and generally makes the spectrum flatter compared to the loss-free spectrum (green curve). The orange curve shows the effect of adding change exchange. It causes depletion below a few hundred keV, where the charge exchange cross section becomes larger. This depletion resembles the spectra that are measured inside of about $L = 8$ in the magnetosphere. Although this seems to suggest that the magnetospheric spectra are shaped by charge exchange, we have not found sufficient evidence to support this theory, as discussed in Appendix A.

Lastly, the red curve in Figure 3 shows the intensity computed when adding the D ring and the energy loss associated with it are included. The ring limits the intensity at large distances from Saturn (Figure 3a). Especially the dense outer part of the ring strongly reduces the intensity. The model shows an intensity maximum around $1.08R_S$, where both the atmosphere and the D ring have a relatively low density. Unfortunately, the model is least reliable at this distance since it depends about equally on atmospheric and ring effects, while at other distances only one is dominant.

Figure 4 shows the relative importance of the different physical processes as a function of energy. The radiation belt around the D ring turns out to have very different characteristics from those of the known belts. The main loss process in the known belts is radial diffusion, driving the protons to the moon orbits . Losses in the Neutral Torus around Enceladus' orbit only play a minor role [*Kollmann et al.*, 2013]. Diffusion turns out to be negligible in the inner belt. Losses are dominated by the interaction with the material. The figure shows the gap region, where this material is largely atmosphere. Energy loss dominates above a few hundred keV and charge exchange below. Since we assume a steady state, these losses balance the source rate exactly. In many cases, energy loss is causing a net particle loss at a given energy ($\hat{E}f < 0$). This is different between 100 and 400 keV, where the spectrum is rising steeply with energy, energy loss is causing a net gain of those protons ($\hat{E}f > 0$).

3.2. Comparison With Known Radiation Belts

In order to simplify the discussion on how the model changes with its parameters we reduce the modeled proton distribution over distance and energy to a single parameter, namely the integral intensity $I = \int j\,\mathrm{d}E\,\mathrm{d}\Omega$, describing the number of protons in an energy range per time and area. We use 10 MeV as the lower energy of the integral since this is a typical value where proton penetration starts to become important. We truncate the integral at 60 MeV because we base our source strength on measurements by the LEMMS instrument [*Kollmann et al.*, 2013], which provides constraints only up to this energy.

Cassini will pass close enough to the planet that the loss cone size (usually very small) becomes relevant, i.e., that the intensity of field-aligned particles becomes almost zero because they bounce into the dense atmosphere and are lost. On the other hand, Cassini remains at high latitude for most of the proximal orbits, so that particles mirroring at lower latitudes do not reach Cassini's location. It turns out that the maximum

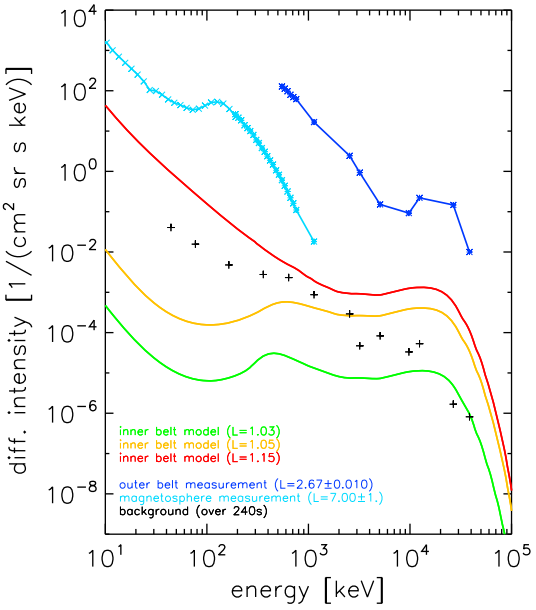

Figure 5. Energy spectra of the model compared with measurements. Green, orange, and red: Modeled spectra assuming the best guess model at distances given in the legend. $L = 1.05$ is an area of relatively high and reliable intensity. (Since the gas density is low and the D ring does not have a strong effect yet.) Blue and cyan: Mission-averaged measurements with the MIMI instrument at locations given in the legend. (We use omnidirectional measurements near the magnetic equatorial plane and average them linearly after applying a median filter. The blue curve shows MIMI/LEMMS alone, the cyan curve a combination with MIMI/CHEMS.) $L = 2.67$ is the region of the most intense radiation observed so far at Saturn, between the orbits of Janus and Mimas. $L = 7$ is an example magnetospheric spectrum. Black: 1 count level of LEMMS when integrating over 240 s.

solid angle with significant intensities during the proximal orbits is $\int d\Omega = 2\pi$. For the calculation of I, we assume that j is constant over this range and zero otherwise.

The default values of our model yield $I = 70 \times 10^5\,m^{-2}s^{-1}$ at the peak of the radiation belt ($L = 1.08$). It is lower in the middle of the D ring ($10 \times 10^5\,m^{-2}s^{-1}$ at $L = 1.03$) and the gap region ($0.1 \times 10^5\,m^{-2}s^{-1}$ at $L = 1.03$ and $4 \times 10^5\,m^{-2}s^{-1}$ at $L = 1.05$). How this changes with the parameters is discussed in section 4.

The most intense proton radiation at Saturn is found in the radiation belt centered at $L = 2.7$, between the orbits of Janus and Mimas and close to the G ring, see Figure 1. This was passed about 14 times by Cassini to date. We interpolate the mission-averaged median measurements in energy and integrate over the energy range given above. This yields $I_{max} = 6 \times 10^8\,m^{-2}s^{-1}$, a value 90 times larger than the default model. When Cassini flew by Earth, it encountered the highest intensities of >10 MeV energies at a radial distance of $1.4R_E$. We linearly fit the energy and integrate it over the given range. This yields a slightly higher value of $10 \times 10^8\,m^{-2}s^{-1}$. It should be noted that this value is not typical for Earth. We only determine it since Cassini passed Earth without issue indicating that this intensity is safe, at least for a single pass. Cassini was designed to withstand even harsher environments with $500 \times 10^8\,m^{-2}s^{-1}$ (Cassini Orbiter Functional Requirements Book, Environmental Design Requirements, November 1996).

While it is possible that the intensity around the D ring is comparable to the known belts, it is also possible that it is too low to be detected at all. A lower limit for detection is the 1 count level, i.e., assuming that an instrument channel receives 1 count while passing this region. A statistically significant signal needs to be well above this. Another difficulty will be determining if the measurement is foreground or contamination from Cassini's radioisotope thermoelectric generators or galactic cosmic rays. We calculate the 1 count level here for a period of 4 min and show it in Figure 5. Four minutes is slightly smaller than the average time that Cassini will be connected to the gap region per orbit. The time connected with the D ring is about 5 times larger, causing an equally smaller 1 count level. It can be seen that our best guess intensity for MeV energies in the D ring and the outer edge of the gap region ($1.05 \lesssim L < 1.24$) is an order of magnitude above the 1 count level, meaning that LEMMS might be able to detect these protons. Based on the uncertainties of the model, we consider it as possible that LEMMS will detect MeV protons also at smaller distances.

4. Parameter Study

Our model predicts for the gap region an intensity well below I_{max} but still above the 1 count level. The intensity in this region depends on the atmospheric density and the source strength, which are relatively well known. Realistic changes in the parameters should not change the result by much more than an order of magnitude. We discuss the details below.

The region magnetically connected with the D ring has much higher intensities that can be comparable to I_{max}. The intensity in this region is known with less certainty than the gap region since the D ring density is poorly constrained. It is easy to justify densities that change the intensity by more than 3 orders of magnitude.

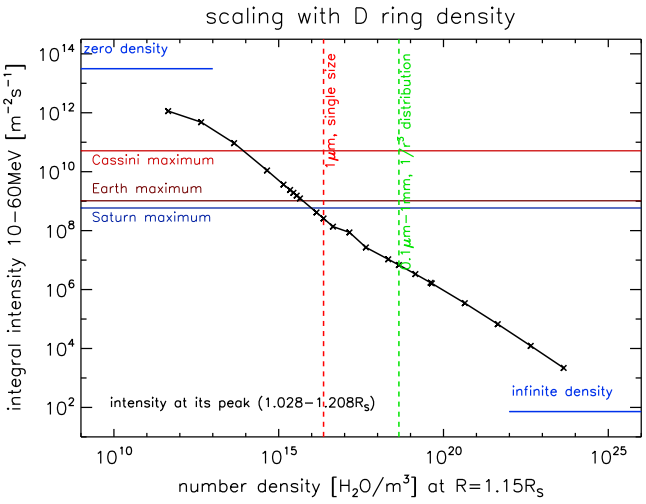

Figure 6. Omnidirectional proton intensity integrated between 10 and 60 MeV. Black curve: Model intensities for different D ring number densities $\langle n \rangle$ at the radial maximum of the radiation belt. The number density $10^{19}/m^3$ converts to $3 \mu g/cm^2$ column density, which is insignificant compared to the tens to hundreds of g/cm^2 of the A and B rings [*Colwell et al.*, 2009b; *Robbins et al.*, 2010]. Realistic values for the D ring should not be too far off the two vertical lines (section 4.1). The red vertical line marks the density resulting from an optical depth of 10^{-4} and grains of 1 μm size. The green vertical line assumes the same optical depth but a power law grain size distribution. The line labeled *Saturn maximum* is the highest intensity so far measured at Saturn (section 3.2). *Earth maximum* is the highest value Cassini experienced during the Earth flyby. *Cassini maximum* is the intensity Cassini is designed to withstand. *Zero density* is the extreme case of no D ring and atmosphere. The intensity is in this case limited by radial diffusion. The intensity for *infinite density* is from transient protons before encountering the ring (section 4.5).

4.1. D Ring Density

The largest uncertainty of our model is the density of the D ring. There is only an upper limit on the optical depth of most of the ring ($<10^{-3}$ inside $1.21R_S$) [*Hedman et al.*, 2007], and the grain size distribution necessary to relate it to its mass density is not well known either. Grain size distributions are commonly power laws roughly following $\overline{n} \propto r^{-3}$ [*Charnoz et al.*, 2009] over a range of $0.1\,m < r < 10\,m$ for the main rings [*Cuzzi et al.*, 2009] and $1\,\mu m < r < 100\,\mu m$ for the tenuous rings (M. M. Hedman, private communication, 2014). The power law will break down at small sizes since small grains can stick to larger grains or leave the Saturn system due to their charge and the corotational electric field. The power law also breaks down at large sizes depending on the grain origin. The locations of these breakdowns are not well known since in optical measurements, the wavelength range constrains the range of grain sizes those wavelengths are most sensitive to. The mass density is insensitive to the lower cutoff ($\langle n \rangle \propto r_{min}^{0.1}$) but sensitive to the upper one ($\langle n \rangle \propto r_{max}^{0.9}$). Lowering the upper cutoff by an order of magnitude will reduce the ring density by almost the same amount. The result is not strongly dependent on the details of the size distribution. Assuming that the size distribution has a sudden change in slope only changes the density by about a factor of 0.5.

Hedman et al. [2007] inferred that the size distribution is narrow. In the outer D ring, it is dominated by 10–100 μm grains while the inner D ring shows 1 μm grains. Assuming that there are only 1 μm grains yields a density that is 100 times lower than what is assumed as our best guess. Using a more realistic Hansen-Hovenir distribution [*Hansen and Hovenier*, 1974; *Hedman et al.*, 2007] instead of a single grain size only changes the prediction by about a factor of 2.

Figure 6 shows the effect of different ring densities on the integral intensity *I*. It can be seen that our default case (r^{-3} size distribution up to 1 mm) yields intensities 100 times below I_{max} while the case of a narrow distribution of 1 μm grains yields intensities that are comparable to I_{max}.

4.2. Atmospheric Density

The atmospheric model was designed to determine the altitude at which the Cassini spacecraft starts to tumble due to atmospheric drag during its last orbit. We use the model in the range where it is supposed to be valid: Tumbling should occur around $1.02R_S$. *Koskinen et al.* [2013] used EUV occultation data to determine the exobase at $1.05R_S$ and the H_2 density up to about $1.06R_S$.

The engineering model uses an upper limit of the *H* density. Despite being a small fraction of the number density near Saturn [*Koskinen et al.*, 2013], *H* becomes highly dominant outside of $1.05R_S$ due to its slower falloff with radial distance. If we assume instead that *H* is always negligible, *I* increases by a factor of 2.

The overall error of the engineering model near the equator is estimated to be smaller than a factor of 2. This is excellent compared to the uncertainties of the other parameters. However, the atmosphere expands and contracts over time [*Koskinen et al.*, 2015] and the density above $1.06R_S$ has not been directly measured.

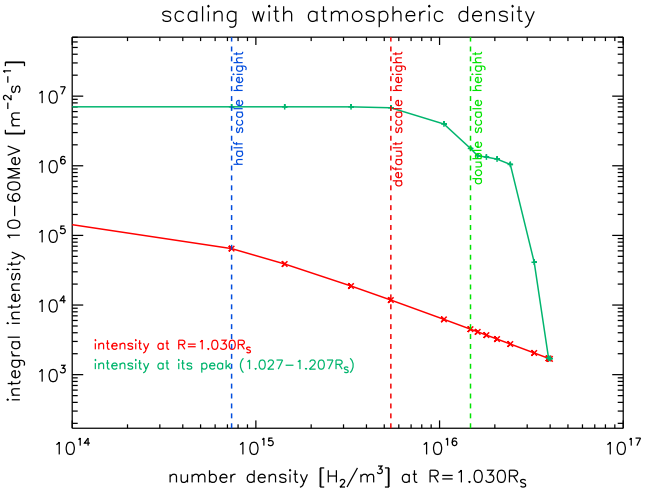

Figure 7. Omnidirectional modeled proton intensities for different scale heights of the thermosphere. Red: Intensity in the gap region, at $R = 1.03$. Green: Maximum intensity in the D ring.

We therefore consider a change in the exponential decay length of H_2 outside of $1.02R_S$. How this affects I is shown in Figure 7. A fast decay causes I to increase near Saturn, but not to a level that would be comparable to the D ring. A slow decay on the other hand will bring down the intensity in the D ring. The atmosphere is therefore not critical for determining the maximum possible intensity I.

4.3. Source

Kollmann et al. [2013] determined the radial power law exponents n and m of the diffusion coefficient and source rate ($S \propto L^{-m}$) in the explored radiation belts. A good fit to the observations required $n + m \approx 14$ and $m \approx 3$ but was not sensitive to the exact values. The results of the current model depend strongly on the scaling of the source and its exponent m. Figure 8 illustrates that an exponent of $m \approx 7$ would cause (with the default D ring density and other parameters) an overall I that is comparable to I_{max}. Such a steep and steady rise is not expected from theory. Theory suggests smaller exponents than we are using. Assuming a low exponent of $m = 1$ or that the source remains constant inside of the distances covered by the *Kollmann et al.* [2013] model yields intensities 1–2 magnitudes below our default case.

We first consider the conceptual cases of isotropic emissions from a sphere or a ring without the presence of a dipole field. The neutron differential intensity j (particles per solid angle, area, time, and energy interval) is constant along the neutron trajectories, which are almost straight lines after leaving the material in which they were created from GCRs. The intensity does not change significantly here because the neutron lifetime is long compared to the time spent near Saturn and the environment around Saturn's atmosphere is tenuous. The omnidirectional intensity (particles per area, time, and energy interval) calculated as $J = \int j d\Omega$ where the integration includes the solid angle covered by the source at any given location. Assuming isotropic, homogenous emission from a sphere of radius R yields immediately $J = 2\pi j(1 - \mathrm{Cos}\{\mathrm{Asin}[R/r]\})$ as a function of distance r to the center. It is $J \approx \pi j R^2/r^2$ for $r \to \infty$ but steepens for $r \to R$, which causes an underestimation of J if a $1/r^2$ extrapolation is used. The solid angle of a disk as a function of arbitrary location was calculated by *Paxton* [1959]. J of a ring can be calculated by subtracting the values of a disk with small radius R_i from a disk with large radius R_o. This yields $J \propto 1/r^2$ for $r \gg R_o$ and $J \propto r$ for $r \ll R_i$ with the distance r from the ring center. This is generally true for all latitudes. Observation near the ring plane shows an additional, relatively strong gradient when approaching the ring edges and flat profile over the ring.

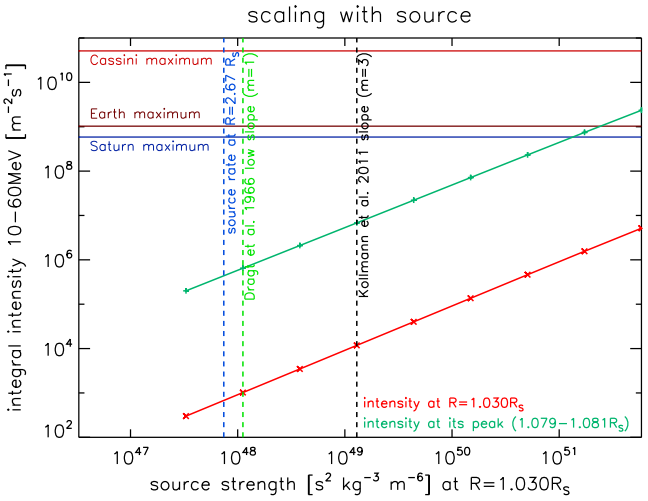

Figure 8. Omnidirectional modeled proton intensities for different radial exponents m of the source. Red: Intensity in the gap region, at $R = 1.03R_S$. Green: Maximum intensity in the D ring. Red vertical line: Exponent of the known radiation belts ($> 2.3R_S$). The value of m changes between neighboring plus and cross symbols by 1. Blue vertical line: Source rate modeled outside of the rings, at $2.67R_S$ [*Kollmann et al.*, 2013]. Green vertical line: The theoretical exponent m ranges between 1 and 2 (section 4). Black vertical line: Modeled exponent [*Kollmann et al.*, 2013].

A proper calculation needs to take into account the magnetic field and provide J as a function of L, not r. All protons created from neutrons on any point of a magnetic field line contribute to the source as long as they have pitch angles that do not correspond to mirror locations deep in the atmosphere. *Cooper* [1983] and *Dragt et al.* [1966] calculated omnidirectional proton intensity (particles per area, time, and energy interval) for different cases of interest, and we fit their results with power laws in L.

Isotropic neutron emission from a sphere scales with an exponent between 1 and 2 at least in the range $1.2 < L < 4$. Anisotropic or inhomogeneous emission mostly from the poles yields an exponent in the same range. It is possible that most neutrons are emitted from Saturn's atmosphere, which can be considered as a spherical source.

There can be important neutron contributions from the rings. Isotropic emission from a flat ring (radial extent from 1.5 to $2.3R_S$) is not described well with a power law over a large L range. Exponents just outside the ring range between 3 and 5. The intensity profile is flatter farther out and above the ring so that extrapolation using the given exponents yields an upper limit. Anisotropic emission modeled from the CRAND process yields, outside the rings ($2.3 < L < 4$), exponents of 4 for > 15 MeV protons and 6 for > 600 MeV [*Cooper*, 1983].

The source rate for transient protons over the rings ($L < 2.3$) can be estimated to actually decrease with an exponent of −2: Only galactic cosmic rays with energies above the Størmer cutoff ($E_c \propto L^{-2}$ for > GeV protons) [*Sauer*, 1980; *Smart and Shea*, 2005] reach the rings. The proton production from cosmic ray protons on oxygen nuclei scales roughly as $S \propto E_c^{-1}$ [*Light et al.*, 1973] and gives rise to a steady state intensity $j \propto S \propto L^2$, consistent with Pioneer observations [*Chenette et al.*, 1980].

4.4. Diffusion

Since diffusion is negligible inside the D ring compared with the strong losses in the neutral material, the diffusion exponent n is not expected to play a major role. Only if the exponent becomes as small as $n \approx 1$, the diffusion rate ($\hat{D}f$ for the solution of equation (2)) becomes comparable to the other rates. Diffusion will act as an additional loss process. It will change the radial profile of the belt and generally decrease its intensity.

4.5. Limiting Cases

In case of unrealistically low densities of the D ring and atmosphere, the intensity will be limited by radial diffusion, as illustrated in Figure 3.

More realistic is the other extreme of a D ring that is sufficiently dense that any proton created is stopped in the ring during its first bounce along the magnetic field lines. This is what happens in the A to C rings. The way we implement source and loss in our model will yield an intensity that approaches zero (Figure 6). This is due to the implicit assumption that energy loss is continuous. In reality, the protons will move freely until the point where they encounter the ring. The intensity of this transient proton population is independent of the ring density, solely determined by the source rate S and the bounce time T_B and can be estimated as ST_B. The result is added to Figure 6. It is small but nonzero.

5. Summary and Conclusions

1. The major loss processes for protons with energies above hundreds of keV in the inner radiation belt are energy loss in the material of the D ring and the planetary atmosphere. Radial diffusion is minor. This is opposite to the known radiation belts.
2. We compare the modeled 10–60 MeV integral intensity with the maximum intensity I_{max} experienced so far at Saturn. The modeled intensity at the outer edge of the gap region ($1.05R_S$) is 3 orders of magnitude below I_{max} and at MeV energies 1 magnitude above the detection threshold of the LEMMS instrument. The uncertainties in this region should not change the result by much more than an order of magnitude.
3. The proton intensity on magnetic field lines connected to the D ring can reach I_{max} for not unreasonable assumptions about the D ring. This intensity should still pose no harm to the spacecraft, especially given the shortness of the exposure times. However, the inner belt of MeV protons could affect scientific measurements, for instance, by contributing background counts in detectors. Due to large uncertainties, it is possible that the intensity is orders of magnitude below I_{max}.
4. Energetic particles might accumulate over the rings at the magnetic equator. These do not bounce to higher latitudes and can therefore only be detected indirectly, e.g., by the remote detection of energetic neutral atoms.

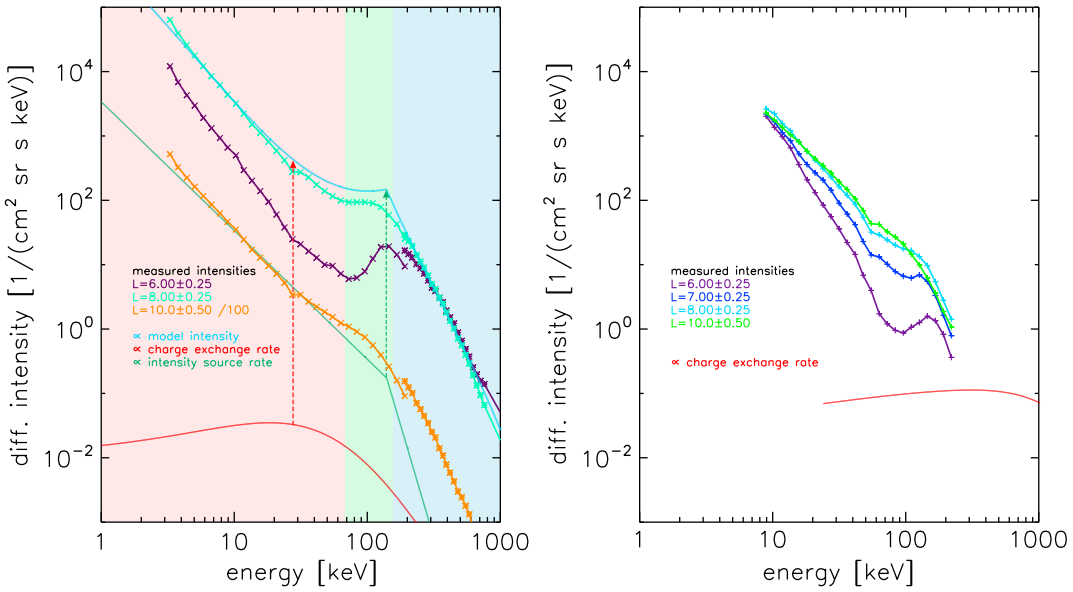

Figure A1. (left) Spectra of protons and (right) water group ions in Saturn's magnetosphere. Water group ions (H_nO^+ with $0 \le n \le 3$) are dominated at these energies by O^+ so we assume them to be oxygen ions. Measurements by the MIMI/CHEMS instrument (cross symbols) and by MIMI/LEMMS (asterisk symbols) of all pitch angles taken within ±10° latitude are linearly averaged throughout the Cassini mission after applying a median filter. The smooth light blue curve in Figure A1 (left) is a model result, and the green curve is the assumed source rate (intensity provided per time). The red curves in both panels show the charge exchange rate (cross section times ion velocity) with water gas. The feature around 100 keV resembles the modeled spectra of the inner belt (Figure 5). It is weaker for oxygen ions when comparing to proton spectra taken at the same distance (see labels). Arrows indicate how the spectral feature is caused by the source and loss processes. The background color marks the three energy ranges that are shown in Figure A2 with similar color coding. Note that instantaneous spectra usually only show a peak around 100 keV. Intensities at lower energies can be in more than half of the cases zero within about $L = 6$. Averaging these zero values with the large, nonzero intensities that occur throughout the mission yields the low-energy power laws shown here. We did not find a consistent change of the spectra with pitch angle but such a dependence might be hidden by the strong variability over the mission.

Appendix A: Charge Exchange in the Magnetosphere

Introducing charge exchange into the model causes an intensity decrease around 100 keV followed by a spectral peak (Figure 3, orange curve). This spectral shape is reminiscent of what is measured in the magnetosphere (Figure A1, left), suggesting that this feature is also caused by charge exchange. The feature in the spectrum is related to a feature of the radial intensity profiles shown in Figure A2. The radial profiles show a peak around $L = 9$ for < 60 keV. Above these energies, approximately where the charge exchange cross sections for protons on the gas of the Enceladus neutral torus falls off, the peak is shifting inward to about $L = 7$. This shift in the radial peak is causing the peak in the spectrum. Understanding the spectra is therefore helpful in understanding the radial distribution.

We solve our model equation (2) for the magnetosphere. The source in this case is not CRAND but radial inward transport from larger distances via radial diffusion (section 2), interchange, and/or dipolarization events [*Arridge et al.*, 2011]. We assume a source spectrum with a shape that resembles the measured spectrum at larger distances. The gas in this region is from the distant portions of the Enceladus neutral torus, which consists predominantly of H_2O and O, depending on distance [*Cassidy and Johnson*, 2010]. We assume charge exchange cross sections for H_2O [*Toburen et al.*, 1968; *Dagnac et al.*, 1970; *Greenwood et al.*, 2000; *Gobet et al.*, 2001], but using O yields similar results. Since the overall source strength is a free parameter here, the result is independent on the assumed neutral density and will only reproduce the spectral shape and not the absolute intensity. The model result shown in Figure A1 roughly agrees with the measured spectrum. The gradient change below 100 keV results from the drop of the charge exchange rate σv around that energy. The second gradient change at slightly higher energies results from the shape we gave the source spectrum S.

While we can reproduce the proton spectra using plausible assumptions, this does not work for the oxygen ion spectra shown in Figure A1, right. The charge exchange rate of oxygen ions is approximately constant over

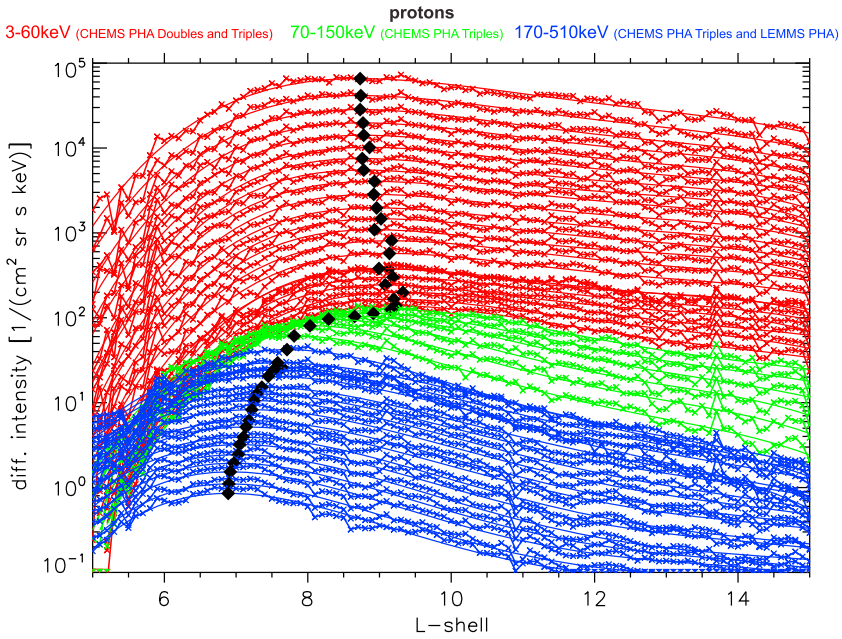

Figure A2. Proton intensity profiles as a function of *L* shell distance to Saturn. Different colors are different energy ranges that use the same color coding as the background shading of the spectra in Figure A1 and are explained further in the legend. Intensities measured throughout the Cassini mission within ±10° latitude are linearly averaged after applying a median filter. Data were taken by the CHEMS and LEMMS instruments. Smooth curves show polynomial fits to the data that were used to determine the radial intensity peak (black solid diamonds) for each energy. While at large distances, low energies (red) have the highest intensities, the shift in the radial peak is causing that large energies (blue) inward of about $L = 7$ have higher intensities than smaller energies (green). This is causing the 100 keV peak in the spectra of this region (Figure A1). Filtering the data for different azimuthal locations shifts the peaks in *L* shell [*Kollmann et al.*, 2011; *Thomsen et al.*, 2012] but roughly the same way for all energies.

the energy range considered here. Reproducing the spectra with a model as above requires that the source alone would need to be responsible for the steady state spectrum. Even if this were a good model, it would mean that the spectral shape is not determined by charge exchange.

There is evidence that energetic protons and oxygen ions are indeed governed by different physics: *Dialynas et al.* [2009] were fitting the spectral peak that is roughly at 100 keV and found that its precise location in energy changes adiabatically with distance to Saturn in case of protons but not of oxygen. However, proton and oxygen spectra are very similar. It is therefore unlikely that charge exchange is the dominant process shaping the proton spectra while a different process is responsible for the oxygen spectra but still results in the same spectral shape. If we doubt the importance of charge exchange for oxygen ions, we therefore need to do the same for protons even though their spectra can be reproduced under this assumption.

It is possible that our inability to establish the importance of charge exchange is because our model is too simplistic. Further analysis should be a topic of further investigation. For now, we would like to point out that even though charge exchange is ongoing (because it is source for the ENAs imaged by MIMI/INCA) [*Krimigis et al.*, 2005, 2007], it does not mean with certainty that it is also the dominant process in shaping the ion distribution.

Appendix B: Discrete Versus Continuous Energy Loss

The change of phase space density at a given energy for particles suffering a continuous energy loss without scattering of their velocity is described in equation (4). An equivalent expression can be found without derivation in *Schulz and Lanzerotti* [1974, equation 2.16, p. 56], and a derivation is given in *Kollmann et al.* [2013]. We consider the other extreme here, namely discrete energy loss that only happens when a projectile hits a target. It is assumed that all targets are spherical grains with diameter $\tilde{X}$. The average distance traversed through each sphere is $X = 2\tilde{X}/3$ since not all grains are hit centrally. The change of proton phase space density f at a given energy E_i per time is determined by (1) the source rate S at this energy, (2) the loss

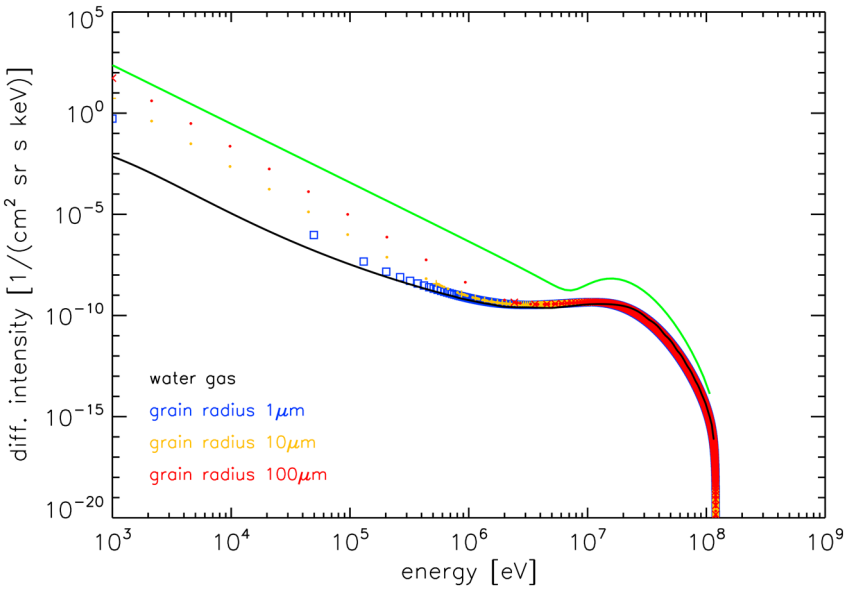

Figure B1. Intensity of protons that are injected into a material with a given spectrum (green curve) and suffer energy loss. Black curve: Resulting proton spectrum if the material is water gas and the protons suffer continuous energy loss. Red, orange, and blue symbols: The water is distributed over ice grains with sizes given in the legend. The distance between large symbols of the same color is due to the discrete energy loss in the ice grains. Energies in between the symbols cannot be reached if the starting energy is $E_E = 120$ MeV. The small dots filling the gaps use slightly different values of E_E.

rate from protons encountering a target grain and losing any nonzero energy in it, and (3) the source from particles with a higher energy E_{i-1} that encounters a target and loses $\Delta = E_{i-1} - E_i$. Expressing this as an equation gives

$$\frac{\mathrm{d}f(E_i)}{\mathrm{d}t} = S(E_i) - \langle n\rangle \sigma v_i f(E_i) + \langle n\rangle \sigma v_{i+1} f(E_{i-1}) \tag{B1}$$

where $\langle n\rangle$ is the grain number density, σ is the geometric grain cross section, and v is the proton velocity (much larger than the grain velocity). This means that $f(E_i)$ can be iteratively calculated after choosing a boundary condition at $i = 0$. We pick $f = 0$ at $E = 120$ MeV in analogy with equation (2). The energy loss Δ is calculated numerically based on the average thickness and the energy loss in the grain $\mathrm{d}E/\mathrm{d}x$:

$$\Delta = \int_0^X \frac{\mathrm{d}E(E)}{\mathrm{d}x}\mathrm{d}x \tag{B2}$$

We show example solutions for different grain sizes in Figure B1 and compare them to equivalent solutions of equation (2) for continuous energy loss. It can be seen that at high energies, where the energy loss per encounter is small, all solutions fall on top of each other. This is the energy range that is of most interest in this paper. The solutions differ from each other at the lower energies. Larger grains cause larger differences.

Acknowledgments
Cassini/MIMI data are available online through NASA's planetary data system (PDS). The JHU/APL authors were partially supported by the NASA Office of Space Science under task order 003 of contract NAS5-97271 between NASA/GSFC and JHU. The MPS authors were partially supported by the German Space Agency (DLR) under contract 50 OH 1502, by the Max Planck Society, and by the International Max Planck Research School for Solar System Science (IMPRS) at the University of Göttingen, Germany and at the Max Planck Institute for Solar System Research (MPS). The authors like to thank D. Strobel (JHU) for developing the engineering atmosphere model, M.M. Hedman (Cornell University) for his analysis on the D ring, A. Lagg (MPS) for analysis software support, and J. Vandegriff (JHU/APL) and M. Kusterer (JHU/APL) for data reduction.

Michael Liemohn thanks Nick Sergis and one another reviewer for their assistance in evaluating this paper.

References

Armstrong, T. P., S. Taherion, J. Manweiler, S. Krimigis, C. Paranicas, D. Mitchell, and N. Krupp (2009), Energetic ions trapped in Saturn's inner magnetosphere, *Planet. Space Sci.*, *57*, 1723–1731, doi:10.1016/j.pss.2009.03.008.

Arridge, C. S., et al. (2011), Mapping magnetospheric equatorial regions at Saturn from Cassini prime mission observations, *Space Sci. Rev.*, *164*, 1–83, doi:10.1007/s11214-011-9850-4.

Barnett, C. F., H. T. Hunter, M. I. Fitzpatrick, I. Alvarez, C. Cisneros, and R. A. Phaneuf (1990), Atomic data for fusion. Volume 1: Collisions of H, H2, He and Li atoms and ions with atoms and molecules, *NASA STI/Recon Tech. Rep. ORNL-6086/V1*, Oak Ridge Natl. Lab., Oak Ridge, Tenn.

Berger, M. J., J. S. Coursey, M. A. Zucker, and J. Chang (2005), *Stopping-Power and Range Tables for Electrons, Protons, and Helium Ions*, Natl. Inst. of Standards and Technol. (NIST), Gaithersburg, Md. [Available at http://www.nist.gov/physlab/data/star.]

Blasi, P. (2013), The origin of galactic cosmic rays, *Astron. Astrophys. Rev.*, *21*, 70, doi:10.1007/s00159-013-0070-7.

Burton, M. E., M. K. Dougherty, and C. T. Russell (2010), Saturn's internal planetary magnetic field, *Geophys. Res. Lett.*, *37*, L24105, doi:10.1029/2010GL045148.

Cassidy, T. A., and R. E. Johnson (2010), Collisional spreading of Enceladus' neutral cloud, *Icarus*, *209*, 696–703, doi:10.1016/j.icarus.2010.04.010.

Charnoz, S., L. Dones, L. W. Esposito, P. R. Estrada, and M. M. Hedman (2009), Origin and evolution of Saturn's ring system, in *Saturn From Cassini-Huygens*, edited by M. K. Dougherty, L. W. Esposito, and S. M. Krimigis, pp. 537–575, Springer, Heidelberg, Germany, doi:10.1007/978-1-4020-9217-6_17.

Chenette, D. L., J. F. Cooper, J. H. Eraker, K. R. Pyle, and J. A. Simpson (1980), High-energy trapped radiation penetrating the rings of Saturn, *J. Geophys. Res.*, *85*, 5785–5792, doi:10.1029/JA085iA11p05785.

Colwell, J. E., J. H. Cooney, L. W. Esposito, and M. Sremčević (2009a), Density waves in Cassini UVIS stellar occultations. 1. The Cassini Division, *Icarus*, *200*, 574–580, doi:10.1016/j.icarus.2008.12.031.

Colwell, J. E., P. D. Nicholson, M. S. Tiscareno, C. D. Murray, R. G. French, and E. A. Marouf (2009b), The structure of Saturn's rings, in *Saturn from Cassini-Huygens*, edited by M. K. Dougherty, L. W. Esposito, and S. M. Krimigis, pp. 375–412, Springer, Heidelberg, Germany, doi:10.1007/978-1-4020-9217-6_13.

Cooper, J. F. (1983), Nuclear cascades in Saturn's rings—Cosmic ray albedo neutron decay and origins of trapped protons in the inner magnetosphere, *J. Geophys. Res.*, *88*, 3945–3954, doi:10.1029/JA088iA05p03945.

Cooper, J. F. (2008), Innermost Van Allen radiation belt for high energy protons at Saturn, *Bull. Am. Astron. Soc.*, *40*(3), 460.

Cooper, J. F., J. H. Eraker, and J. A. Simpson (1985), The secondary radiation under Saturn's A-B-C rings produced by cosmic ray interactions, *J. Geophys. Res.*, *90*, 3415–3427, doi:10.1029/JA090iA04p03415.

Cooper, J. F., A. S. Lipatov, E. C. Sittler, and S. J. Sturner (2011), Saturn neutron exosphere as source for inner and innermost radiation belts. Geophysical Research Abstracts Vol. 13, EGU2011-12735 presented at EGU General Assembly Conference 2011.

Cuzzi, J., R. Clark, G. Filacchione, R. French, R. Johnson, E. Marouf, and L. Spilker (2009), Ring particle composition and size distribution, in *Saturn from Cassini-Huygens*, edited by M. K. Dougherty, L. W. Esposito, and S. M. Krimigis, pp. 459–509, Springer, Heidelberg, Germany, doi:10.1007/978-1-4020-9217-6_15.

Dagnac, R., D. Blanc, and D. Molina (1970), A study on the collision of hydrogen ions H_1^+, H_2^+ and H_3^+ with a water-vapour target, *J. Phys. B*, *3*, 1239–1251, doi:10.1088/0022-3700/3/9/007.

Dialynas, K., S. M. Krimigis, D. G. Mitchell, D. C. Hamilton, N. Krupp, and P. C. Brandt (2009), Energetic ion spectral characteristics in the Saturnian magnetosphere using Cassini/MIMI measurements, *J. Geophys. Res.*, *114*, A01212, doi:10.1029/2008JA013761.

Dragt, A. J., M. M. Austin, and R. S. White (1966), Cosmic ray and solar proton albedo neutron decay injection, *J. Geophys. Res.*, *71*, 1293–1304.

Elrod, M. K., W.-L. Tseng, R. J. Wilson, and R. E. Johnson (2012), Seasonal variations in Saturn's plasma between the main rings and Enceladus, *J. Geophys. Res.*, *117*, A03207, doi:10.1029/2011JA017332.

Esposito, L. W., et al. (2004), The Cassini ultraviolet imaging spectrograph investigation, *Space Sci. Rev.*, *115*, 299–361, doi:10.1007/s11214-004-1455-8.

Gobet, F., B. Farizon, M. Farizon, M. J. Gaillard, M. Carré, M. Lezius, P. Scheier, and T. D. Märk (2001), Total, partial, and electron-capture cross sections for ionization of water vapor by 20–150 keV protons, *Phys. Rev. Lett.*, *86*, 3751–3754, doi:10.1103/PhysRevLett.86.3751.

Greenwood, J. B., A. Chutjian, and S. J. Smith (2000), Measurements of absolute, single charge-exchange cross sections of H^+, He^+ and He^{2+} with H_2O and CO_2, *Astrophys. J.*, *529*, 605–609, doi:10.1086/308254.

Gusev, A. A., G. I. Pugacheva, U. B. Jayanthi, and N. Schuch (2003), Modeling of low-altitude quasi-trapped proton fluxes at the equatorial inner magnetosphere, *Braz. J. Phys.*, *33*, 775–781.

Hansen, J. E., and J. W. Hovenier (1974), Interpretation of the polarization of Venus, *J. Atmos. Sci.*, *31*, 1137–1160, doi:10.1175/1520-0469(1974)031<1137:IOTPOV>2.0.CO;2.

Hedman, M. M., et al. (2007), Saturn's dynamic D ring, *Icarus*, *188*, 89–107, doi:10.1016/j.icarus.2006.11.017.

Hess, W. N., H. W. Patterson, R. Wallace, and E. L. Chupp (1959), Cosmic-ray neutron energy spectrum, *Phys. Rev.*, *116*, 445–457, doi:10.1103/PhysRev.116.445.

Horányi, M., J. A. Burns, M. M. Hedman, G. H. Jones, and S. Kempf (2009), Diffuse rings, in *Saturn from Cassini-Huygens*, edited by M. K. Dougherty, L. W. Esposito, and S. M. Krimigis, pp. 511–536, Springer, Heidelberg, Germany, doi:10.1007/978-1-4020-9217-616.

Kollmann, P., E. Roussos, C. Paranicas, N. Krupp, C. M. Jackman, E. Kirsch, and K.-H. Glassmeier (2011), Energetic particle phase space densities at Saturn: Cassini observations and interpretations, *J. Geophys. Res.*, *116*, A05222, doi:10.1029/2010JA016221.

Kollmann, P., E. Roussos, C. Paranicas, N. Krupp, and D. K. Haggerty (2013), Processes forming and sustaining Saturn's proton radiation belts, *Icarus*, *222*, 323–341, doi:10.1016/j.icarus.2012.10.033.

Koskinen, T. T., B. R. Sandel, R. V. Yelle, F. J. Capalbo, G. M. Holsclaw, W. E. McClintock, and S. Edgington (2013), The density and temperature structure near the exobase of Saturn from Cassini UVIS solar occultations, *Icarus*, *226*, 1318–1330, doi:10.1016/j.icarus.2013.07.037.

Koskinen, T. T., B. R. Sandel, R. V. Yelle, D. F. Strobel, I. C. F. Müller-Wodarg, and J. T. Erwin (2015), Saturn's variable thermosphere from Cassini/UVIS occultations, *Icarus*, *260*, 174–189, doi:10.1016/j.icarus.2015.07.008.

Kreussler, S., and R. Sizmann (1982), Neutralization of 50–230 keV hydrogen ions which have penetrated Al, Au, C, and Cs films, *Phys. Rev. B*, *26*, 520–529, doi:10.1103/PhysRevB.26.520.

Krimigis, S. M., and T. P. Armstrong (1982), Two-component proton spectra in the inner Saturnian magnetosphere, *Geophys. Res. Lett.*, *9*, 1143–1146, doi:10.1029/GL009i010p01143.

Krimigis, S. M., J. F. Carbary, E. P. Keath, T. P. Armstrong, L. J. Lanzerotti, and G. Gloeckler (1983), General characteristics of hot plasma and energetic particles in the Saturnian magnetosphere: Results from the Voyager spacecraft, *J. Geophys. Res.*, *88*, 8633–8634.

Krimigis, S. M., et al. (2004), Magnetosphere Imaging Instrument (MIMI) on the cassini mission to Saturn/Titan, *Space Sci. Rev.*, *114*, 233–329, doi:10.1007/s11214-004-1410-8.

Krimigis, S. M., et al. (2005), Dynamics of Saturn's magnetosphere from MIMI during Cassini's orbital insertion, *Science*, *307*, 1270–1273, doi:10.1126/science.1105978.

Krimigis, S. M., N. Sergis, D. G. Mitchell, D. C. Hamilton, and N. Krupp (2007), A dynamic, rotating ring current around Saturn, *Nature*, *450*, 1050–1053, doi:10.1038/nature06425.

Light, E. S., M. Merker, H. J. Verschell, R. B. Mendell, and S. A. Korff (1973), Time dependent worldwide distribution of atmospheric neutrons and of their products: 2. Calculation, *J. Geophys. Res.*, *78*, 2741–2762, doi:10.1029/JA078i016p02741.

Lindsay, B. G., and R. F. Stebbings (2005), Charge transfer cross sections for energetic neutral atom data analysis, *J. Geophys. Res.*, *110*, A12213, doi:10.1029/2005JA011298.

Moritz, J. (1972), Energetic protons at low equatorial altitudes, *Z. Geophys.*, *38*, 701–717.

Paxton, F. (1959), Solid angle calculation for a circular disk, *Rev. Sci. Instrum.*, *30*, 254–258, doi:10.1063/1.1716590.

Robbins, S. J., G. R. Stewart, M. C. Lewis, J. E. Colwell, and M. Sremčević (2010), Estimating the masses of Saturn's A and B rings from high-optical depth N-body simulations and stellar occultations, *Icarus*, *206*, 431–445, doi:10.1016/j.icarus.2009.09.012.

Roederer, J. G. (1970), *Dynamics of Geomagnetically Trapped Radiation*, Springer, Heidelberg, Germany.

Roussos, E., N. Krupp, T. P. Armstrong, C. Paranicas, D. G. Mitchell, S. M. Krimigis, G. H. Jones, K. Dialynas, N. Sergis, and D. C. Hamilton (2008), Discovery of a transient radiation belt at Saturn, *Geophys. Res. Lett.*, *35*, L22106, doi:10.1029/2008GL035767.

Roussos, E., N. Krupp, C. P. Paranicas, P. Kollmann, D. G. Mitchell, S. M. Krimigis, T. P. Armstrong, D. R. Went, M. K. Dougherty, and G. H. Jones (2011), Long- and short-term variability of Saturn's ionic radiation belts, *J. Geophys. Res.*, *116*, A02217, doi:10.1029/2010JA015954.

Sauer, H. H. (1980), On Saturnian cosmic ray cutoff rigidities, *Geophys. Res. Lett.*, *7*, 215–217, doi:10.1029/GL007i003p00215.

Schulz, M., and L. J. Lanzerotti (1974), Particle diffusion in the radiation belts, in *Physics and Chemistry in Space*, vol. 7, edited by J. G. Roederer, 1st ed., Springer, Heidelberg, Germany.

Seidelmann, P. K., et al. (2007), Report of the IAU/IAG Working Group on cartographic coordinates and rotational elements: 2006, *Celestial Mech. Dyn. Astron.*, *98*, 155–180, doi:10.1007/s10569-007-9072-y.

Simpson, J. A., T. S. Bastian, D. L. Chenette, R. B. McKibben, and K. R. Pyle (1980), The trapped radiations of Saturn and their absorption by satellites and rings, *J. Geophys. Res.*, *85*, 5731–5762, doi:10.1029/JA085iA11p05731.

Singer, S. F. (1958), Trapped albedo theory of the radiation belt, *Phys. Rev. Lett.*, *1*, 181–183, doi:10.1103/PhysRevLett.1.181.

Smart, D. F., and M. A. Shea (2005), A review of geomagnetic cutoff rigidities for Earth-orbiting spacecraft, *Adv. Space Res.*, *36*, 2012–2020, doi:10.1016/j.asr.2004.09.015.

Thomsen, M. F., E. Roussos, M. Andriopoulou, P. Kollmann, C. S. Arridge, C. P. Paranicas, D. A. Gurnett, R. L. Powell, R. L. Tokar, and D. T. Young (2012), Saturn's inner magnetospheric convection pattern: Further evidence, *J. Geophys. Res.*, *117*, A09208, doi:10.1029/2011JA017482.

Toburen, L. H., M. Y. Nakai, and R. A. Langley (1968), Measurement of high-energy charge-transfer cross sections for incident protons and atomic hydrogen in various gases, *Phys. Rev.*, *171*, 114–122, doi:10.1103/PhysRev.171.114.

Waite, J. H., et al. (2006), Cassini ion and neutral mass spectrometer: Enceladus plume composition and structure, *Science*, *311*, 1419–1422, doi:10.1126/science.1121290.

Walt, M. (1994), *Introduction to Geomagnetically Trapped Radiation*, 1st ed., Cambridge Univ. Press, Cambridge, U. K.

Wolfram Research (2012), Mathematica 9, commercial software. [Available at http://www.wolfram.com/.]